

Oxygen-rich tetrahedral surface phase on high-temperature rutile VO₂(110)_T single crystals

Margareta Wagner^{1,*}, Jakub Planer^{1,2}, Bettina S. J. Heller³, Jens Langer⁴, Andreas Limbeck⁵, Lynn A. Boatner⁶, Hans-Peter Steinrück³, Josef Redinger^{1,2}, Florian Maier³, Florian Mittendorfer^{1,2}, Michael Schmid¹ and Ulrike Diebold¹

¹Institute of Applied Physics, TU Wien, Wiedner Hauptstraße 8–10/134, 1040 Vienna, Austria

²Center for Computational Materials Science, TU Wien, Wiedner Hauptstraße 8–10/134, 1040 Vienna, Austria

³Physical Chemistry II, Friedrich-Alexander-Universität Erlangen-Nürnberg (FAU), Egerlandstrasse 3, 91058, Erlangen, Germany

⁴Inorganic and Organometallic Chemistry, Friedrich-Alexander-Universität Erlangen-Nürnberg (FAU), Egerlandstrasse 1, 91058 Erlangen, Germany

⁵Institute of Chemical Technologies and Analytics, TU Wien, Getreidemarkt 9/164, 1060 Vienna, Austria

⁶Materials Science and Technology Division, Oak Ridge National Laboratory, Oak Ridge, Tennessee 37831, USA



(Received 15 June 2021; accepted 8 October 2021; published 2 December 2021)

Vanadium dioxide undergoes a metal-insulator transition from an insulating (monoclinic) to a metallic (tetragonal) phase close to room temperature, which makes it a promising functional material for many applications, e.g., as chemical sensors. Not much is known about its surface and interface properties, although these are critical in many applications. In this paper, we present an atomic-scale investigation of the tetragonal rutile VO₂(110)_T single-crystal surface and report results obtained with scanning tunneling microscopy, low-energy electron diffraction, and x-ray photoelectron spectroscopy, supported by density-functional-theory-based calculations. The surface reconstructs into an oxygen-rich (2 × 2) superstructure that coexists with small patches of the underlying unreconstructed (110)-(1 × 1) surface when the crystal is annealed >600 °C. The best structural model for the (2 × 2) surface termination, conceptually derived from a vanadium pentoxide (001) monolayer, consists of rings of corner-shared tetrahedra. Over a wide range of oxygen chemical potentials, this reconstruction is more stable than the unreconstructed (110) surface and models proposed in the literature.

DOI: [10.1103/PhysRevMaterials.5.125001](https://doi.org/10.1103/PhysRevMaterials.5.125001)

I. INTRODUCTION

Vanadium(IV) dioxide, VO₂, undergoes a first-order metal-to-insulator transition (MIT) at a temperature T_C of ~ 67 °C, where the lattice changes from the insulating monoclinic structure M1 (distorted rutile) to the metallic, tetragonal (rutile) structure above T_C [1]. The MIT shows a hysteresis of several Kelvin in heating and cooling cycles. An intermediate strain- or doping-induced monoclinic phase M2 has been observed during the phase transition, together with a metastable triclinic phase occurring between M1 and M2 [2,3]. The physical mechanism behind the complex phase transition of this strongly correlated oxide is still controversially discussed; an overview is given in Ref. [4].

VO₂ is technologically interesting, as its MIT occurs near room temperature. The change in resistivity by several orders of magnitude is accompanied by changes in optical, thermal, and magnetic properties. The MIT can be tailored to ultrafast switching in the range of ~ 500 fs [5,6], and

recently, ~ 26 fs was reported by Jager *et al.* [7]. Moreover, lattice strain [8], also induced by cation or hydrogen doping [9–11], electric current, electric field gating, and irradiation with light [12] modify the MIT and shift its transition temperature even closer to room temperature. The properties and tunability of the MIT in VO₂ are employed in applications, e.g., in memristive devices [13], optical modulators [14], gas sensors [15], field-effect transistors [16], or smart window coatings [17,18].

Since surface properties play an essential role in many of these applications, several recent studies have characterized VO₂ surfaces, predominantly using supported thin and ultrathin films. It was revealed [19,20] that tensile (compressive) strain along the rutile c axis imposed by a lattice mismatch with the substrate is correlated with an increase (decrease) in transition temperature. Recent evidence points toward a selvage concentration of oxygen atoms at the surface not only in the ambient environment [21] but also under reducing conditions comparable with ultrahigh vacuum (UHV) [22]. Moreover, density functional theory (DFT) calculations [23] revealed that tetragonal surfaces are lower in energy than their monoclinic counterparts. Also, oxygen-rich reconstructions reduce the occupation of surface $3d$ states, an important driving parameter for the MIT [24]. These findings are consistent with surface-sensitive low-energy electron diffraction (LEED) measurements [23,25], which revealed no evidence of the bulk structural transition to the monoclinic phase at the surface

*Corresponding author: wagner@iap.tuwien.ac.at

Published by the American Physical Society under the terms of the [Creative Commons Attribution 4.0 International](https://creativecommons.org/licenses/by/4.0/) license. Further distribution of this work must maintain attribution to the author(s) and the published article's title, journal citation, and DOI.

when the sample was cooled down below the transition temperature.

These recent results call for detailed knowledge of the atomic-scale structure of VO₂ surfaces. Such information can be gained by applying complementary surface science techniques to single crystals and combining these experiments with DFT calculations. In this paper, we focus on the (110)_T (tetragonal) surface of VO₂ above T_C , where the high electrical conductivity enables such experiments. It starts with a thorough bulk characterization of the structure and purity of the VO₂ single crystals grown from the melt. The experiments were quite challenging; the MIT relates to a massive structural change. The rigid sample mount required for the surface science measurements can easily fracture the samples during the phase transition; therefore, the crystals were kept at elevated temperatures throughout most experiments.

LEED confirms the (2 × 2) periodicity observed in earlier works [23,26]. X-ray photoelectron spectroscopy (XPS) supports that the surface is a vanadium oxide phase enriched with oxygen compared with the bulk and excludes the possibility of impurity segregation. Atomically resolved scanning tunneling microscopy (STM) studies show that the (2 × 2) structure consists of an adlayer on top of the (1 × 1). A detailed analysis of these results constrains the possible structural models.

From the DFT perspective, vanadium dioxide is a challenging material due to strong electron-electron correlations. Benchmark calculations show that standard DFT functionals cannot correctly describe bulk properties like the electron density, relative phase stability, band gap, and magnetic ordering for both the rutile and monoclinic phases at the same time [27,28]. Nevertheless, DFT was successfully employed to characterize the surface structure of several VO_x-derived surfaces. For example, Schoiswohl *et al.* [29] characterized the formation of ultrathin VO_x structures on a metallic substrate with a combination of atomically resolved STM and *ab initio* calculations, which provided additional information on the exact stoichiometry or the atomistic structure. Klein *et al.* [30] investigated V₂O₃ and V₅O₁₄ structures on Pd(111) and confirmed the structures obtained with DFT experimentally by LEED-I(V). DFT calculations were also employed in the structural and energetic characterization of V₂O₅ and V₆O₁₃(001) surfaces [31].

In this paper, DFT is used to interpret the experimental observations, and a tetrahedrally coordinated surface phase is the best fit to the experimental results.

II. MATERIALS AND METHODS

A. Samples

The VO₂ single crystals were grown from the melt using V₂O₅ powder kept in Ar flow at 1000 °C for 120 h inside a quartz crucible. The solid black crystals were shaped as needles or thin plates of ~2–10 mm length, 1–4 mm in width, and <1 mm in thickness, exposing a flat and reflective top side; see Fig. 1(a). Larger crystals often consisted of several smaller needles grown together. The crystals were brittle and broke easily during mounting. Figure 1(b) shows a crystal tightly mounted on a Ta sample plate with a single Ta spring for STM measurements. A thin Au foil was placed between the crystal

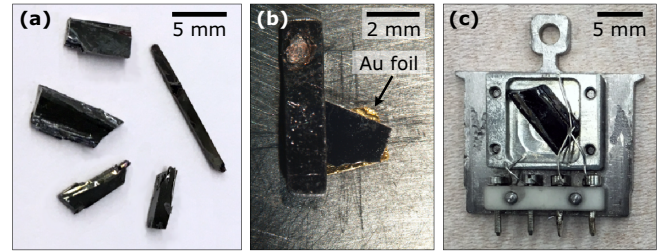


FIG. 1. The VO₂ single crystals. (a) A selection of large, as-grown crystals exposing the flat and shiny side. Small crystals are usually needle shaped, like the rightmost crystal in the picture. (b) A crystal mounted for scanning tunneling microscopy (STM) measurements, held tightly by a tantalum spring and gold foil. (c) A crystal mounted in a heated molybdenum sample holder for x-ray photoelectron spectroscopy (XPS) measurements, with a thermocouple on top and held in place by an additional Chromel wire.

and sample plate to improve thermal contact to the rough backside of the crystal. The crystal broke into several pieces after a week of measurements, which also involved multiple sample transfers inside the UHV chamber. Panel (c) shows one of the larger crystals prepared for XPS measurements. It was placed inside the recess of a molybdenum sample holder; the crystal was gently held by a 0.2 mm Chromel wire, spot-welded to the edges of the recess. A Chromel-alumel thermocouple was connected to the crystal.

B. Bulk impurities

The purity of the crystals was investigated by trace analysis with laser ablation inductively coupled plasma mass spectrometry (LA-ICP-MS). All crystals showed a constant ⁵¹V signal across the whole surface (1–2 mm) and traces of Ba (<2.3 ppm), Pb (<7 ppm), U (0.25–41 ppm), Mg (<0.42 ppm), Al (0.03–81 ppm), Ta (0.03–302 ppm), and Au (0.0–58 ppm); see the Supplemental Material [32]. The impurities were different for each crystal and showed inhomogeneous distributions across the individual crystals. The Au and Ta signals were particularly high on a crystal that had been previously sputtered in UHV, mounted with a Ta spring on a Ta sample plate with an Au foil underneath the sample [Fig. 1(b)].

C. Structural characterization

X-ray diffraction (XRD) was employed to confirm the bulk structures above and below the transition temperature and to determine the surface orientation of the shiny crystal side. The diffractometer requires small samples; hence, it was necessary to cut the original VO₂ single crystals into appropriate pieces. A selected fragment is shown in Figs. 2(a) and 2(b); its longest side measures 0.35 mm. Several crystals were investigated, both as grown and after the XPS measurements (discussed below), which included crossing the phase transition a few times and heating in UHV to 650 °C. As expected, the treatment in UHV did not influence the bulk structure, although it introduced twin formation. The data were processed with the CRYCALISPRO (v38.46) software package [33], and unit cell

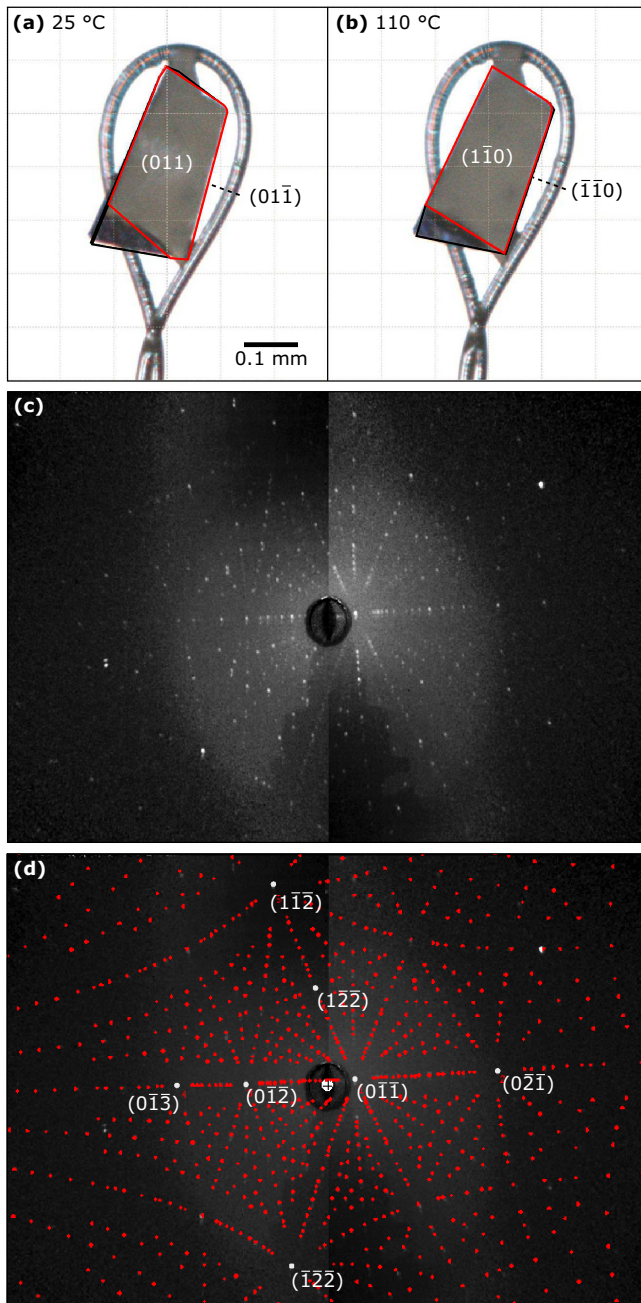


FIG. 2. Determination of the surface orientation. (a) and (b) Crystal fragment investigated with x-ray diffraction (XRD) for temperatures below and above the metal-to-insulator transition (MIT), respectively. The experimentally obtained Miller indices of several crystallographic planes are indicated for each case. (c) Laue back-reflection of the monoclinic phase at room temperature with the sample rotated slightly out of normal incidence. (d) The same pattern superimposed by a fit.

determination confirmed the known monoclinic modification at 25 °C, while the tetragonal form was present at 110 °C.

In addition to the XRD study and to verify the crystal quality and orientation, Laue back-reflection analysis was applied to some crystals before the STM measurements [Figs. 2(c) and 2(d)].

D. Surface techniques

The surface properties of the VO₂ single crystals were investigated with XPS, LEED, and STM. The XPS measurements were conducted in a UHV chamber equipped with two hemispherical analyzers (Omicron ARGUS) in 80° geometry with overlapping detection areas described elsewhere [34]. This setup allowed for simultaneous acquisition of normal- and grazing-emission spectra using focused monochromatic Al K α x rays (1486.6 eV; Omicron XM 1000).

The STM and LEED experiments were performed in two different UHV systems: (1) a two-chamber UHV system consisting of an analysis chamber (base pressure 1×10^{-10} mbar) equipped with a variable-temperature STM (Aarhus 150, SPECS), a multichannel plate (MCP) LEED (SpectaLEED, Omicron), and a preparation chamber (base pressure $<5 \times 10^{-10}$ mbar) for sample cleaning and preparation purposes and (2) a two-chamber UHV system consisting of an analysis chamber (base pressure 2×10^{-11} mbar) equipped with a low-temperature STM (Omicron LT-STM) and an adjacent preparation chamber (base pressure 5×10^{-11} mbar) containing LEED and sample cleaning facilities. Both STMs used etched W tips, and the STM heads were maintained at a temperature of 80 °C during the experiments. The STM images shown in this paper were acquired at a bias voltage $\sim +2$ V, which is suitable for stable imaging of this surface.

E. Surface measurement procedures

For the measurements in UHV, the crystals were inserted into the chambers via a small side chamber without bakeout to minimize the number of phase transitions. It was found that each phase transition shortened the lifetime of the crystals significantly. However, even when minimizing the transitions, the crystals eventually broke along grain boundaries, most likely due to mechanical stress during transfers inside the vacuum chamber and the forces applied by the mounting process. Thus, after the first heating above the MIT temperature, the VO₂ crystals were always held at 200–250 °C, i.e., also during sputtering, LEED, XPS measurements, and overnight. In both STM UHV chambers, the surface of the VO₂ crystals was initially cleaned by several cycles of sputtering (1 keV Ar⁺ ions, $\sim 2.5 \mu\text{A}/\text{cm}^2$, 10 min) and annealing in UHV (10 min). In the chamber with the variable-temperature STM, the annealing temperature was determined as >600 °C measured on the crystal and ~ 700 °C measured on the Ta sample plate, both using a pyrometer with an emissivity set to 0.8. In the LT-STM system, the annealing temperature of ~ 600 °C was measured via a thermocouple. The surface was daily refreshed either by an entire cleaning cycle or by annealing. Variations in the sample preparation, which did not change the surface according to STM examination, included annealing at 600 °C in 2×10^{-6} mbar O₂ combined with cooling in O₂ until the temperature decreased to 300 °C, annealing in 1×10^{-8} mbar H₂ at 450 °C, and dosing 10 Langmuir (L, 1 L = 1.33×10^{-6} mbar · s) of water into the STM at 80 °C. In the XPS chamber, the crystals were sputtered for 60 min (1 keV Ar⁺ ions, $\sim 8 \mu\text{A}/\text{cm}^2$) followed by annealing at 350–700 °C for 10 min. The samples were sputtered before each annealing step to reset the history of the surface.

TABLE I. Structural parameters of the VO₂ phases below and above the transition temperature $T_C = 67^\circ\text{C}$ [42,43].

Crystal system	Space group	T (K)	a (Å)	b (Å)	c (Å)	α, γ (°)	β (°)
Monoclinic (M1)	$P2_1/C$	300	5.75	4.53	5.38	90	122.6
Tetragonal (T)	$P4_2/mmm$	360	4.55	4.55	2.85	90	90.0

F. DFT calculations

All calculations were performed with the Vienna *ab initio* Simulation Package (VASP) [35]. The projector-augmented wave method [36] was employed for treating core electrons. For oxygen, six valence electrons ($2s^2 2p^4$) and, for vanadium, 13 valence electrons ($3s^2 3p^6 3d^4 4s^1$) were expanded in a plane-wave basis set with an energy cutoff set to 500 eV. As this paper is focused on the metallic rutile phase, we chose a DFT-based description using the meta-generalized gradient approximation (meta-GGA) strongly constrained and appropriately normed (SCAN) functional [37]. This functional was reported [38] as the best compromise between computational cost and accuracy in terms of lattice parameters and relative phase stability for the rutile and monoclinic VO₂ phases. In this paper, all calculations were performed assuming nonmagnetic VO₂ systems. While a recent study suggested a better description of the surface energies [23] with spin-polarized calculations, we found that the influence on the present results is rather small. A detailed discussion of these findings, together with a critical assessment of the performance of various DFT functionals for this system, is presented elsewhere [39].

The Brillouin zone was sampled with a Γ -centered Monkhorst-Pack grid [40], using $6 \times 6 \times 9$ k-points for the bulk rutile phase. For surface calculations, the k-points grid was adjusted to obtain a comparable sampling of the surface Brillouin zone. Ionic relaxations were stopped when all residual forces became $< 10^{-2}$ eV/Å. All slabs were calculated with lateral cell dimensions corresponding to the optimized bulk lattice constants with a separating vacuum layer kept at 15 Å.

While the surface energies of the (1×1) terminations were calculated from a linear fit of the total energies vs slab thickness from 5 to 8 layers, the surface free energies of the off-stoichiometric (2×2) surface terminations were calculated using five-layer slabs with symmetric top and bottom surfaces and the bulk energy derived from the (1×1) slabs. All simulated STM images were generated in the Tersoff-Hamann approximation [41] with a bias voltage of +2 eV. To obtain a more accurate description of the charge density in these calculations, the energy cutoff was increased by 30% with respect to the other calculations.

III. RESULTS AND DISCUSSION

A. Diffraction results

Before discussing the diffraction results, it is useful to recall the crystallographic relationship between the monoclinic and tetragonal phases. The lattice parameters of both phases are summarized in Table I. The transition of a crystallographic plane characterized by $(hkl)_T$ to a monoclinic (M) plane is

described in Ref. [42] by

$$\begin{pmatrix} h \\ k \\ l \end{pmatrix}_M = \begin{pmatrix} 0 & 0 & -2 \\ -1 & 0 & 0 \\ 0 & 1 & 1 \end{pmatrix} \begin{pmatrix} h \\ k \\ l \end{pmatrix}_T.$$

Thus, for example, $(0\bar{1}\bar{1})_M$ transforms into $(1\bar{1}0)_T \equiv (110)_T$, $(\bar{2}\bar{1}2)_M$ into $(111)_T$, and $(\bar{2}02)_M$ into $(011)_T$.

The orientation of the shiny side of the crystals was determined by XRD (both the monoclinic and tetragonal phase), Laue back-reflection (RT, monoclinic phase), as well as LEED (200 °C, tetragonal phase). In XRD, see Figs. 2(a) and 2(b), the face marked by a red line corresponds to the monoclinic $(011)_M$ plane at 25 °C and the tetragonal $(1\bar{1}0)_T$ plane at 110 °C, respectively. For all crystals, the best match for the obtained Laue diffraction pattern is the $(0\bar{1}\bar{1})_M$ surface, and an example is given in Figs. 2(c) and 2(d), which corresponds to $(110)_T$ above T_C .

In UHV, the first LEED experiments with conventional LEED optics showed a rectangular pattern above T_C that vanished very quickly, although no typical charging effects were observed. In the MCP LEED (~ 26 nA/mm²), the pattern was stable for at least half an hour. The LEED images of Figs. 3(a) and 3(b), obtained after annealing the sample at 600 °C, show a (2×2) superstructure. This superstructure is discussed in more detail in the STM section. Less intense satellites next to the main diffraction spots in Fig. 3(a) originate from the differently tilted macroscopic crystallites that were present in most samples. Some diffraction spots associated with the reconstruction vanish at specific energies, indicated by white circles in Fig. 3(b). The ratio of the surface lattice parameters taken from the LEED images $a_s^*/b_s^* \approx 2.3$ matches the

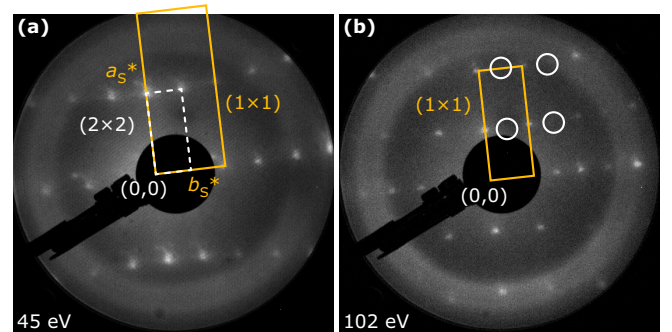


FIG. 3. Low-energy electron diffraction (LEED) pattern of the rutile phase at 200 °C taken at two different electron energies. The (1×1) pattern (solid orange rectangle) of a $(110)_T$ termination and the (2×2) superstructure (dashed white rectangle) are indicated. Note that some reflections of the superstructure are not present in the image taken at 102 eV (white circles). Weak satellite spots are due to mosaicity.

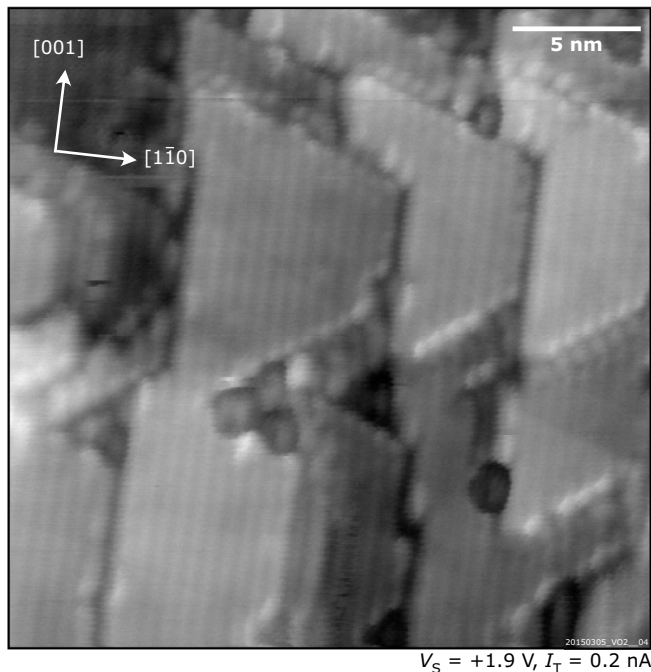


FIG. 4. The $\text{VO}_2(110)_T$ surface after annealing at 560°C , showing only the (1×1) surface without any superstructures in empty-states scanning tunneling microscopy (STM).

expected value of the $(110)_T$ surface $b_S/a_S = \sqrt{2}a/c = 2.26$ (see also Table I).

B. Scanning tunneling microscopy

The surface structure observed in STM evolved with the annealing temperature after the sputter treatment. While the (1×1) structure is observed after mild annealing at $\sim 560^\circ\text{C}$, different superstructures emerge at higher temperatures. An-

nealing the crystal at $\sim 560^\circ\text{C}$ leads to a rather rough surface with terraces of only 5–10 nm size. On the terraces, the structure of rutile $\text{VO}_2(110)$ is observed. This is shown in Fig. 4, where the atomic rows of the $(110)_T$ surface running in the $[100]$ direction are clearly visible. The absence of mirror symmetry in the island shape and the high step density suggest screw dislocations due to an STM tip crash nearby.

After annealing at $>600^\circ\text{C}$, the surface exhibits terraces that are larger than after annealing at 560°C , see Fig. 5. The single-layer step height of $\text{VO}_2(110)_T$, ~ 320 pm, was used to calibrate the z distances. (This was necessary, as the calibration of the piezo characteristics is usually done at room temperature and can be different at the elevated temperatures used in these STM measurements). In addition to the unreconstructed $\text{VO}_2(110)_T(1 \times 1)$ surface, two superstructures are found: a (2×2) and a $c(4 \times 2)$ overlayer; the latter was always on top of the (2×2) structure and is associated with Cs impurities of most crystals, discussed later. Both structures were present on all crystals after annealing at $>600^\circ\text{C}$, but their coverages varied. In fact, the $c(4 \times 2)$ structure seems to influence the formation of the (2×2) phase: the higher the coverage of the $c(4 \times 2)$ structure, the lower the coverage of the (2×2) phase and the more (1×1) surface remains, see Figs. 5 and S4 in the Supplemental Material [32]. In the following, the (2×2) superstructure is described in detail to capture all features relevant for DFT modeling.

The primary superstructure is an adlayer with (2×2) symmetry in agreement with the LEED pattern. Figure 5 shows images obtained on two different crystals where the coverage of the (2×2) layer varies from $\sim 30\%$ to $\sim 100\%$ and, accordingly, the coverage of the $c(4 \times 2)$ from 20% to single atoms. On most crystals, the larger part of the surface was covered by the (2×2) structure, and the $\text{VO}_2(110)_T(1 \times 1)$ surface was found only at step edges or in small holes of the adlayer. The apparent height of the (2×2) structure on top of the $\text{VO}_2(110)$ terrace measures ~ 160 pm. At step

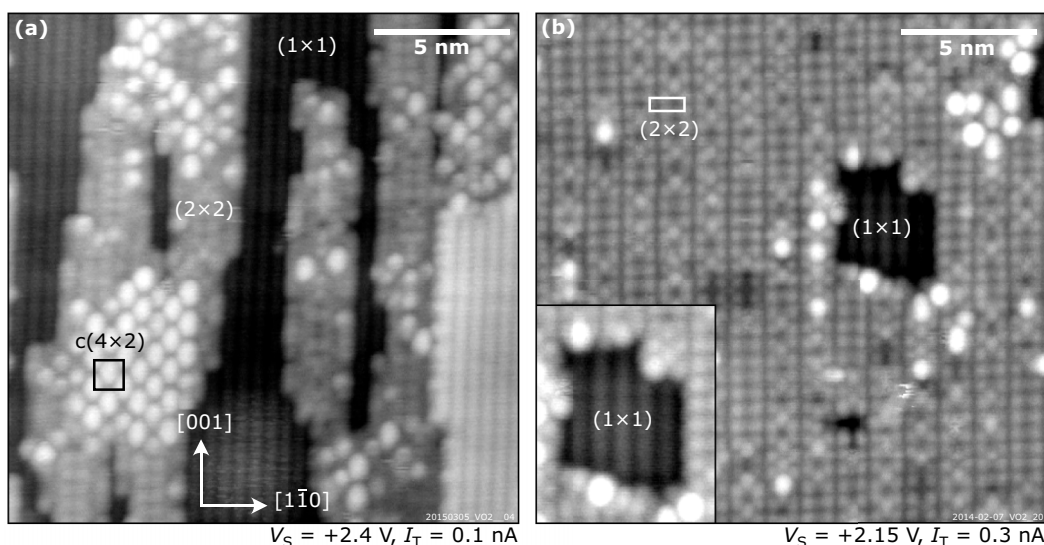


FIG. 5. Scanning tunneling microscopy (STM) measurements on two different $\text{VO}_2(110)_T$ crystals acquired at 80°C . (a) Crystal with step edges along the $[001]$ direction showing the unreconstructed $\text{VO}_2(110)_T(1 \times 1)$ surface, narrow stripes of the (2×2) , and patches of the $c(4 \times 2)$ phase on top of the (2×2) . (b) Crystal with an almost complete overlayer of the (2×2) phase; holes in the (2×2) layer reveal $\text{VO}_2(110)_T(1 \times 1)$.

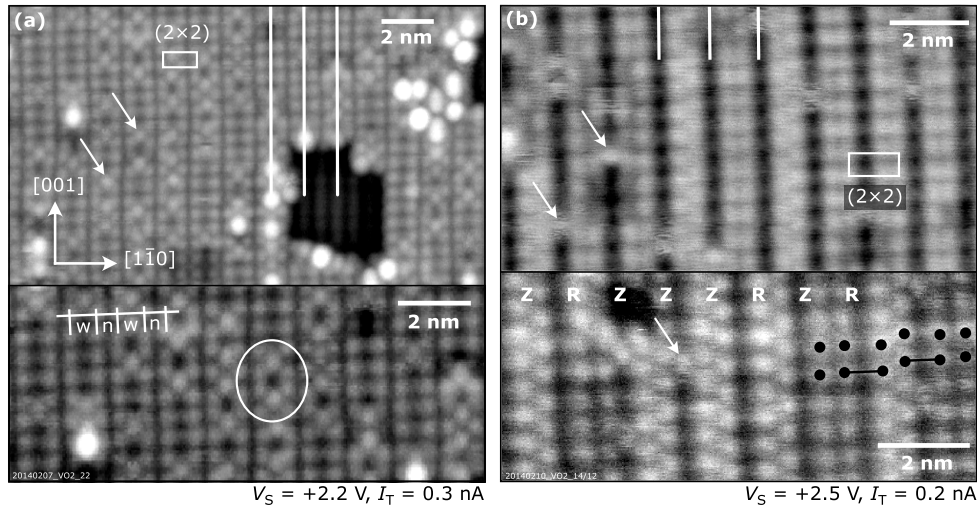


FIG. 6. Scanning tunneling microscopy (STM) contrasts and details of the (2×2) row structure. White markers in the top part of the panels indicate the positions of the wide spacing between the double rows. Comparison of (a) with (b) shows that contrast does not always emphasize the wide spacing as the main depression. Additional features situated in the wide sites are marked by white arrows. (a) The alignment of the wide spacing with respect to the bright rows of the VO_2 surface visible inside the holes is indicated. (b) Distinct double-row structure with domain boundaries (displacements within the double row along $[100]$), resulting in lines with zigzag (Z) structure, in contrast to the usual rectangular (R) arrangement.

edges of the (1×1) terraces, the (2×2) adlayer always grows on top of the lower terrace, regardless of the step orientation; usually, it does not cover the terrace completely, especially when a high coverage of the $c(4 \times 2)$ is present. At first glance, the (2×2) structure consists of double rows parallel to the $[001]$ direction, i.e., two narrow-spaced rows separated by a wider spacing. Figure 6 provides STM images of this structure displaying the two most prominent and purely tip-related contrasts; other appearances are provided in the Supplemental Material [32]. Moreover, the structures and additional features are not sensitive to the bias voltage or its polarity. Note that the distances of the wide and narrow spacing strongly depend on the tip configuration (see Table S3 and Fig. S5 in the Supplemental Material [32]), which makes accurate geometry determinations difficult. The space between the double rows can be decorated with three different features, which do not depend on the imaging contrast of the (2×2) structure. They are all imaged as single protrusions seemingly sitting in a fourfold hollow site of the wide spacing. The first species is an additional dot with a similar apparent height as the row maxima. These features often occupy every other fourfold hollow site along the rows, leading to flowerlike features [white ellipse in Fig. 6(a)]. The second feature is a protrusion in the same site but with a fuzzy appearance that also includes the four neighboring protrusions of the (2×2) structure (indicated by white arrows in Fig. 6). Both species are stable during image acquisition and do not diffuse at 80°C . Finally, there are also a few very bright protrusions close to this site [Fig. 6(a)], which form the $c(4 \times 2)$ structure if their coverage is sufficiently high.

All these features can be used to identify the wide spacing of the (2×2) double rows even if the rows appear equidistant. White lines at the top parts of Fig. 6 mark the wide spacing. Measuring the distances of the individual protrusions within the $\times 2$ periodicity along the $[1\bar{1}0]$ direction reveals different

spacings for all observed tip-related contrasts (Figs. 6 and S5 in the Supplemental Material [32]). The structure in Fig. 6(b) contains domain boundaries along the $[001]$ direction. The bottom panel of Fig. 6(b) shows that these domain boundaries result in a zigzag (Z) arrangement of protrusions along the rows instead of the expected rectangular (R) pattern. It should be noted that the two rows framing the wide spacing are always aligned in the $[1\bar{1}0]$ direction [indicated by connected dots in the inset of Fig. 6(d)], and the zigzag is always within the narrow-spaced double row.

The consistent alignment of the (2×2) double rows with respect to the bright rows of the $\text{VO}_2(110)\text{-}(1 \times 1)$ surface (discussed below), together with the identical features visible between the row pairs in all contrasts, strongly indicate that all the structures presented in Fig. 6 are, in fact, identical. The zigzag rows are the result of defective regions such as shifted building blocks or domain boundaries.

The alignment of the (2×2) with respect to the (1×1) structure is evaluated in Fig. 7. Along the $[001]$ direction, both the narrow and the wide spacings of the (2×2) structure are centered on the bright rows of the $\text{VO}_2(110)\text{-}(1 \times 1)$ area, see white and orange lines in Fig. 7(b). Inside the hole, where the $\text{VO}_2(110)\text{-}(1 \times 1)$ is visible, the white lines of the (2×2) grid in $[1\bar{1}0]$ direction are in between the protrusions of the $\text{VO}_2\text{-}(1 \times 1)$ rows. The white and yellow lines together form the (1×1) structure. Along $[1\bar{1}0]$, the protrusions of the (2×2) structure are centered on every second line (yellow); hence, they are in between the protrusions observed in the $\text{VO}_2(110)$ area.

The $c(4 \times 2)$ superstructure is often less prominent than (2×2) and not visible in the LEED pattern due to its small domains. It is a centered rectangular arrangement formed by bright, slightly elongated protrusions with lattice constants of ~ 1.14 nm and ~ 1.29 nm, corresponding to a $c(4 \times 2)$ periodicity with respect to $\text{VO}_2(110)\text{-}(1 \times 1)$ or a $c(2 \times 1)$

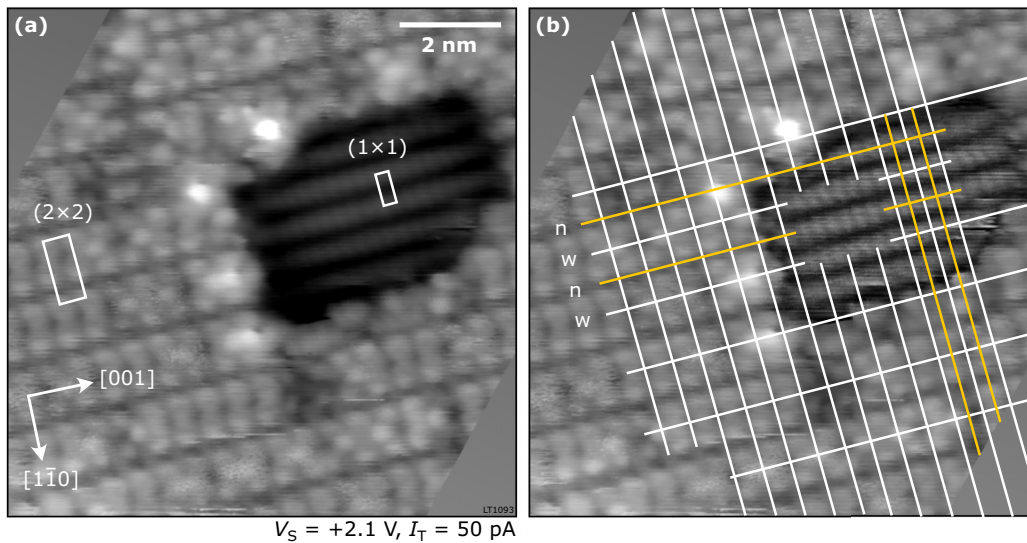


FIG. 7. Alignment of the (2×2) structure with respect to the $\text{VO}_2(110)_T(1 \times 1)$. The scanning tunneling microscopy (STM) image of panel (b) is the same as in (a) with a high-pass filter applied to the (1×1) region. The grids in (b) are centered on the (1×1) rows and offset by $\frac{1}{2}[001]$ with respect to the maxima of these rows). Further explanations are given in the text.

with respect to (2×2) . This structure is always on top of the (2×2) layer and never on the $\text{VO}_2(1 \times 1)$ patches, although these protrusions are preferentially found in the vicinity of edges and holes in the (2×2) layer [Fig. 5(b)]. Figure 5(a) shows a very high coverage of this structure, where half of (2×2) is covered. This structure is tentatively assigned to Cs impurities segregating to the surface, which were found in the XPS spectra discussed below.

C. XPS: Chemical composition

The surface and near-surface region of larger crystals was systematically investigated at different annealing temperatures after cleaning by sputtering. The aim was to see whether the (2×2) and the $c(4 \times 2)$ structures are due to a stoichiometrically different vanadium-oxide phase or possibly related to the segregation of impurities. The investigated temperature range was 250–700 °C, and the measurements were repeated on five crystals from different batches. The main impurity seen on these samples was Cs, segregating at the surface above 450 °C with Cs $3d_{5/2}$ and Cs $3d_{3/2}$ peaks at 738.5 and 724.5 eV, respectively. After annealing at 650 °C, the Cs concentration was calculated for Cs $3d_{5/2}$ vs O $1s$ and V $2p$ using atomic sensitivity factors. It ranged from 0.1 to 2.3% in the normal emission XPS spectra and from 0.3 to 6.0% in the respective grazing emission data and stayed constant for each crystal during the experiments. It was not possible to influence the Cs concentration by excessive sputtering and annealing cycles or sputtering at 600 °C. The XPS data shown in Fig. 8 were obtained on a crystal with <1% Cs both in normal and grazing emission. Moreover, SiO_2 (Si $2p$ at ~ 103 eV and an additional O $1s$ shoulder at ~ 533.5 eV), and occasionally, small amounts of Ni (originating from the thermocouple wire holding the crystals), Ar (incorporated during sputtering, normal emission only), Mo (sample holder, in grazing emission only), and K (with a concentration of 0.2–0.6% in normal emission and 0.7–2.0% in grazing emission; calculated for K

$2p$ vs O $1s$ and V $2p$ using atomic sensitivity factors) were observed. The SiO_2 originates from the quartz crucible the VO_2 crystals were grown in; on some samples, discolored edges and backsides were found, possibly related to this impurity. Si was not detected in the trace analysis (LA-ICP-MS) across the samples used for STM because these samples were selected to be without any visual fault.

The evolution of the vanadium and oxygen core levels was followed with XPS as a function of the annealing temperature from 350 to 700 °C by simultaneously acquiring grazing emission (80 °) and normal-emission (0 °) spectra. Figure 8 displays the evolution of the O $1s$ and V $2p$ states measured at 200 °C, i.e., tetragonal $\text{VO}_2(110)$. The spectra are normalized with respect to the background on the low-binding-energy side. Moreover, the binding energy of the O $1s$ peak is set to 530.0 eV for better comparison, compensating a gradual shift of total ~ 1.5 eV to lower binding energies; see Fig. S7(c) in the Supplemental Material [32]. The V $2p$ core-level spectra are complex in both grazing and normal emission [Figs. 8(a) and 8(b), respectively], suggesting several oxidation states. Overall, the O $1s$ intensity increases relative to the V $2p$ intensity with increasing temperature. Quantitative fitting of these spectra is beyond the scope of this paper, as one would have to consider possible oxidation-state-dependent satellite features of the V $2p$ levels, which overlap with the O $1s$ region and thus strongly affect the deconvolution into various components. Nevertheless, qualitative information can be deduced and allow for comparing these data with results from the literature. Reported V $2p_{3/2}$ binding energies for different oxidation states vary from ~ 512.35 eV for V(0) to ~ 517.20 eV for V(V) (with the O $1s$ located at 530 eV) [44,45]. With increasing annealing temperature, the V $2p$ signals in Fig. 8 shift to higher binding energies. At 350 °C (black spectra), where the surface is still roughened from the ion bombardment, oxidation states range from metallic V(0) to V(V), with mostly metallic and low oxidation states. At 450 °C (red) the V $2p_{3/2}$ feature centers around V(III)

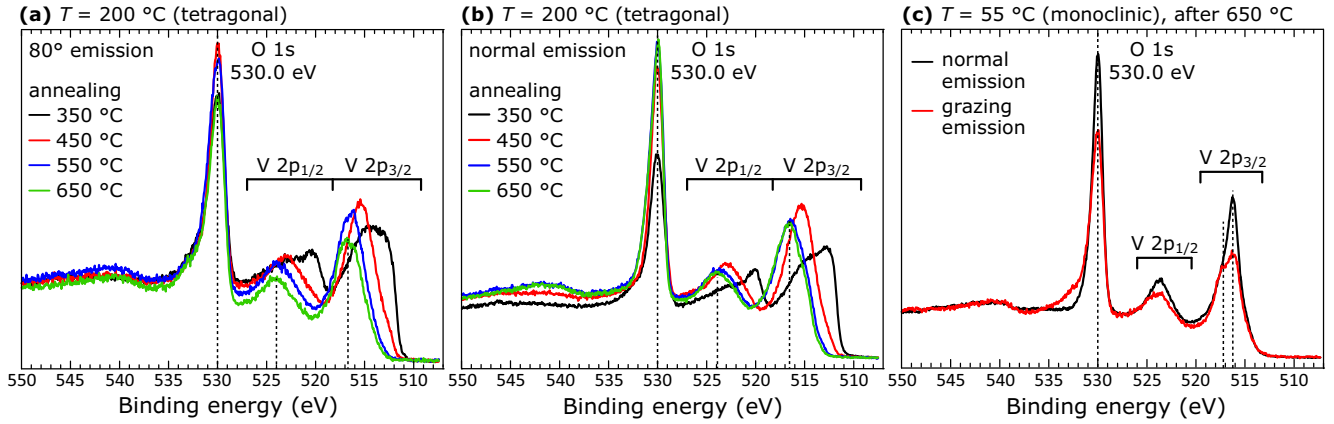


FIG. 8. Temperature-dependent x-ray photoelectron spectroscopy (XPS) core-level spectroscopy of a VO_2 single crystal. (a) and (b) The $\text{VO}_2(110)_T$ phase after annealing in ultrahigh vacuum (UHV) at different temperatures. The surface was sputtered before each annealing step. All spectra were acquired at 200 °C in (a) grazing emission and (b) normal emission. (c) Normal and grazing emission spectra obtained on the monoclinic phase at 55 °C, after annealing at 650 °C [green curves in (a) and (b)]. All spectra were shifted to obtain a common O 1s binding energy of 530 eV.

(~ 515.3 eV), with a shoulder toward the metallic side. At temperatures of 550 °C (blue) and higher (650 °C, green), the V $2p_{3/2}$ binding energy lies between those of V(IV) and V(V) (~ 515.8 and ~ 517.2 eV, respectively [44]), indicating a mixture of these oxidation states. The comparison of normal and grazing emission data reveals a small shift (0.1–0.2 eV) of the V $2p_{3/2}$ and V $2p_{1/2}$ signals toward higher binding energies at 80°, indicating higher oxidation states at the surface; see also Fig. S6 in the Supplemental Material [32].

In Fig. 8(c), the monoclinic phase was investigated with XPS [46] by preparing the sample at 650 °C and cooling below the MIT temperature to 55 °C. Spectra obtained by this procedure essentially display the same oxidation states as in the tetragonal phase but with a different peak shape due to the different screening in the metallic and insulating phases [47]. A plot comparing the tetragonal and monoclinic spectra is provided in Fig. S7 in the Supplemental Material [32].

D. DFT: The $(110)_T$ - (1×1) and $(011)_T$ - (1×1) terminations of rutile VO_2

The slab calculations were performed with the optimized bulk lattice constants presented in Table II. The SCAN functional correctly predicts the rutile phase to be metallic. While the calculated cell size in the basal plane (a) agrees with experiment, the calculated lattice vector c (and thus the cell volume and c/a ratio) is underestimated by $\sim 3\%$. The calculated lattice parameters are in perfect agreement with previous reports for the same functional [38].

The stability of the unreconstructed low-index facets of the rutile phase $(110)_T$ and $(011)_T$ was evaluated by calculating

their respective surface energies (Table II), finding the (110) surface to be more stable by $36 \text{ meV}/\text{\AA}^2$.

The bulk-terminated, relaxed surfaces of rutile $\text{VO}_2(110)_T$ and $\text{VO}_2(011)_T$ are shown in Figs. 9(a) and 9(b), respectively. In calculated STM images of the $\text{VO}_2(110)_T$ -terminated surface, Fig. 9(c), the twofold-coordinated oxygen atoms appear as straight, bright chains with a distance of 6.45 Å. This appearance differs from the well-known $\text{TiO}_2(110)$ surface, where the bridging oxygen rows appear dark [48], but it is the same as that for $\text{RuO}_2(110)$, which is also metallic [49]. Both the appearance of rows and their separation are in agreement with experimental STM images of $\text{VO}_2(110)_T$ - (1×1) in Figs. 4 and 5. The bright features on the $\text{VO}_2(011)_T$ termination, Fig. 9(d), are formed by both vanadium and oxygen atoms, resulting in zigzag chains.

E. Developing a surface model

To investigate possible reconstructions of the bare $\text{VO}_2(110)_T$ surface, a simulated annealing technique was employed. A subsequent relaxation with the SCAN functional shows that even for the bare $\text{VO}_2(110)_T$ surface, the calculated ground state has its symmetry lowered due to buckling in the topmost layer, resulting in a (2×1) superstructure (Fig. 10, shown together with a simulated STM image). The surface reconstruction is formed by the displacement of vanadium atoms along the $[110]$ direction, leading to a relative height difference of 0.31 Å between the vanadium atoms. Nevertheless, with an energy gain of only 80 meV per (2×1) unit cell, the buckled ground state is almost degenerate with the unreconstructed surface termination. As a side note, other GGA and meta-GGA functionals also

TABLE II. Calculated parameters of the rutile unit cell and the surface energies σ of VO_2 , using the meta-GGA (SCAN) functional.

	a (Å)	c (Å)	c/a	V (Å ³)	$\sigma_{(110)}$ (meV/Å ²)	$\sigma_{(011)}$ (meV/Å ²)
SCAN (this paper)	4.56	2.77	0.61	28.81	40	76
Experiment [42,43]	4.55	2.85	0.63	29.54	—	—

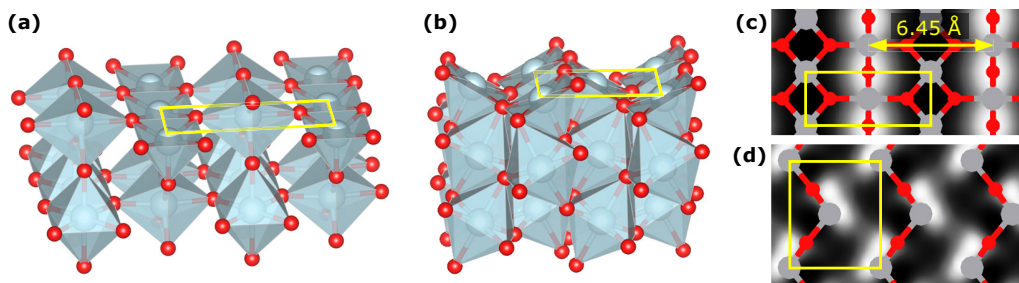


FIG. 9. Side views and simulated scanning tunneling microscopy (STM) images (empty states) of (a) and (c) the $\text{VO}_2(110)_T$ and (b) and (d) the $\text{VO}_2(011)_T$ bulk terminations using the Tersoff-Hamann approximation.

predict a similar trend: using PBE, PBE + $U(U - J = 2 \text{ eV})$, and SCAN + rVV10 functionals, the buckling stabilizes the surface by 75, 39, and 34 meV, respectively.

A molecular dynamics simulation performed at a temperature of 350 K with four-layer slabs to reduce the computational effort showed that the vanadium pairs flip from the up-down to the down-up configuration and vice versa with an average flipping time of 200 fs. Since STM measurements show time-averaged data and the flipping time is far below the resolution limit, this buckled superstructure will exhibit the same STM image as an unbuckled $\text{VO}_2(110)_T$ surface.

A hint guiding one toward an appropriate atomic model for the (2×2) structure can be derived from the experimental findings, which suggest a surface stoichiometry different from the bulk: Our XPS measurements indicate an increased concentration of O on the surface and the presence of V^{5+} cations. In addition, the experimental STM images of the (2×2) resemble patterns found on the $\text{V}_2\text{O}_5(001)$ surface as characterized by Blum *et al.* [31], suggesting that a vanadium pentoxide monolayer might be a good starting point for the development of an atomic model. We take the orientation of the V_2O_5 lattice such that the cleavage plane is (001), i.e., the $\text{V} = \text{O}$ vanadyl bonds are roughly parallel to [001]. To fit the $\text{VO}_2(110)_T$ substrate in a (2×2) configuration, the unit cell of the $\text{V}_2\text{O}_5(001)$ monolayer needs to be expanded in the [100] direction from 11.50 to 12.86 Å (i.e., by 12%), breaking up the structure along the dashed symmetry plane [see Fig. 11(a)], and in the [010] direction from 3.56 to 5.70 Å (i.e., by 60%). This strong distortion leads to the rearrangement of the V_2O_5 building blocks, namely, a change from

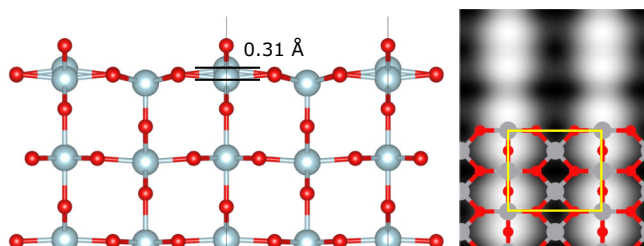


FIG. 10. Buckled superstructure on $\text{VO}_2(110)_T$ and the corresponding calculated scanning tunneling microscopy (STM) image. The structure was obtained by simulated annealing and relaxed using the SCAN functional. Bright spots in the simulated STM image are formed by the topmost oxygen row. Note that all oxygen atoms have the same height.

edge-sharing pyramids to corner-sharing tetrahedra. The dark vanadium polyhedra pointing away from the surface (toward the vacuum) shift along the [010] direction, and the inverted (bright) polyhedra are pulled toward each other in the [100] direction. This is marked by yellow arrows in Fig. 11(a). The result is a hexagonal ring of vanadium tetrahedra, as shown in Fig. 11(b). A similar structure consisting of corner-sharing up- and down-pointing VO_4 tetrahedra has already been confirmed for vanadium oxide on a Pd(111) surface [30]. For the unsupported model layer [Fig. 11(b)], the lateral distance between the oxygen atoms at the top of the tetrahedra along $[1\bar{1}0]$ is 3.8 Å. When this layer is supported by the rutile $\text{VO}_2(110)_T$ surface, as shown in Figs. 11(c) and 11(d), the distance is slightly decreased to 3.7 and 3.6 Å, respectively. In both cases, the surface has an overall stoichiometry of V_4O_{13} .

Figures 11(c) and 11(d) show two different configurations indicating how the structure could be placed on the VO_2 substrate underneath. In the first case, panel (c), the ring termination is bound in a corner-sharing fashion, i.e., with just one oxygen bond, forming a purely tetrahedral termination and leaving half of the undercoordinated O atoms of the substrate unterminated. These atoms, colored in orange, can also be partly or entirely removed, which leads to V_4O_{12} and V_4O_{11} surface stoichiometries. In Fig. 11(d), the ring termination is shifted by a half of the (1×1) rutile [001] lattice vector, as marked with the orange arrow. The additional bond to the undercoordinated O atoms of the substrate layer converts the lower tetrahedra to square pyramids (black circles in panels (c) and (d)). This shift stabilizes the surface termination by 0.24 eV per (2×2) supercell. Figure 11(e) shows a simulated STM image of the ring structure from Fig. 11(d). The calculated STM contrasts were also studied at different bias voltages between -2 and $+2$ V. The bright spots are always formed by oxygen atoms (see Figs. S9(a)–9(d) in the Supplemental Material [32]). This finding indicates that the geometric height of the oxygen atoms dominates the contrast in the calculated STM images. The ring pattern can be transformed into another stable structure, shown in Figs. 11(f) and 11(g), by two major changes. First, the rings are connected by another vanadium tetrahedron (pink), thereby changing the surface stoichiometry to V_5O_{14} . Second, half of the dark tetrahedra are bound to the substrate layer, while the other tetrahedra are moved to the surface layer [light gray in Figs. 11(f) and 11(g)]. The V_5O_{14} configuration is, therefore, structurally like the $\text{SrTiO}_3(110)$ termination that is shown as the (3×1) surface structure in Ref. [50] but with two major

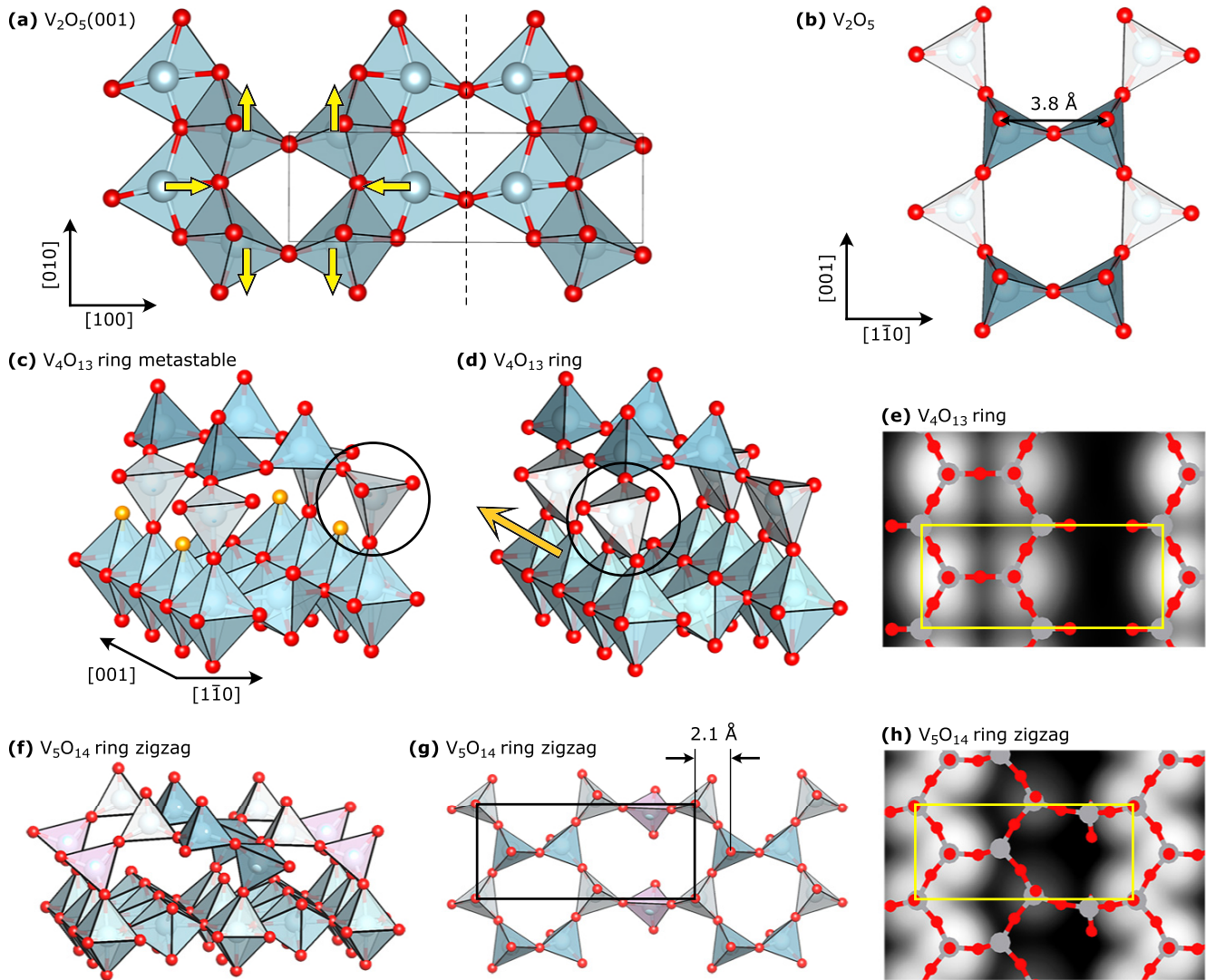


FIG. 11. Conceptual steps toward the $\text{VO}_2(110)_T$ ring terminations. (a) A vanadium pentoxide (001) monolayer. The yellow arrows mark the displacement direction of the vanadium atoms, which causes the transformation to the tetrahedral ring superstructure that fits the $\text{VO}_2(110)_T$ - (2×2) supercell, shown in (b). (c) and (d) Side views of two possible connections of this ring structure with the underlying $\text{VO}_2(110)_T$ lattice, resulting in an overall stoichiometry of V_4O_{13} . The purely tetrahedral ring termination (c) contains in the subsurface layer $\text{V}=\text{O}$ vanadyl bonds that can be subsequently removed (oxygen atoms colored in orange). The difference between the structures in (c) and (d) is a shift along the $[001]$ direction as pointed out with the yellow arrow in (d), changing the coordination geometry of marked vanadium atoms from tetrahedra to square pyramids. The configuration in (d) is lower in energy than the structure in (c). (e) A calculated scanning tunneling microscopy (STM) image of the ring structure in (d). (f) and (g) Side and top views of another ring termination that can be derived from (b). The calculated STM image of this structure is shown in (h).

differences. The first difference is related to the bonding of the superstructure to the bulk termination. Second, in the case of VO_2 some vanadium tetrahedra are terminated with another oxygen atom, which disconnects them from the (110) surface, and vanadyl bonds are formed on top (see Fig. S5 in the Supplemental Material [32]). This modified ring structure results in a zigzag STM pattern, shown in Fig. 11(h). The bright spots are separated by 2.1 \AA (projected in the $[1\bar{1}0]$ direction, see Fig. 11(g)). Note that the experimental data show large variations of this spacing depending on the condition of the STM tip; thus, a direct comparison of experimental and theoretical values is not possible. The simulated STM image in Fig. 11(f) shows an additional subtle spot that comes from the second row of upward-pointing tetrahedra. The height difference of

the topmost oxygen atoms between the rows made of upward-pointing tetrahedra is $\sim 1 \text{ \AA}$; thus, the low-lying protrusions are not expected to be observed in the experiment. All ring structures of Figs. 11(c)–11(f) are significantly thicker than a rutile $\text{VO}_2(110)_T$ layer (3.3 \AA), measuring 5.5 , 5.4 , and 5.8 \AA , respectively.

To explain the additional features in the STM images, other metastable ring-type structures were also explored. In these structures, an additional vanadium tetrahedron was added between the rows of the ring structure in Fig. 11(c), which changes the stoichiometry of the surface layer (V_5O_{14} and V_5O_{15}); these structures are less stable than those in Figs. 11(c)–11(h). Details are discussed in the Supplemental Material [32].

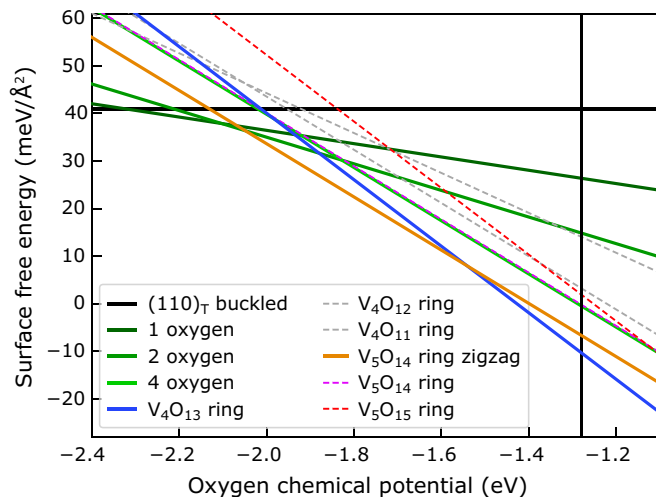


FIG. 12. Calculated surface free energies (SCAN functional) of the $\text{VO}_2(110)_T$ surface as a function of the oxygen chemical potential. Shown are the buckled $\text{VO}_2(110)_T$ termination [from Fig. 10(a), black line], oxygen adsorption on the buckled $(110)_T$ surface (green lines), and the ring terminations from Figs. 11(d) (blue line), 11(f) (orange line), and S8(a) and S8(b) in the Supplemental Material [32] (dashed lines). Gray dashed lines represent the reduced ring terminations with V_4O_{12} and V_4O_{11} surface stoichiometry. They were obtained from the V_4O_{13} structure in Fig. 11(c) by subsequently removing the orange oxygen atoms from the subsurface layer, leading to V_4O_{12} and V_4O_{11} surface stoichiometry. The solid black vertical line represents the experimental stability limit of VO_2 with respect to the vanadium pentoxide phase.

F. Stability of surface phases

To evaluate the stability of various surface terminations, we plotted the surface free energy as a function of the oxygen chemical potential as it is described in Ref. [51]—see Fig. 12. The black horizontal line represents the stoichiometric buckled $\text{VO}_2(110)_T$ surface. Green lines denote (2×2) supercells of this buckled surface with 1, 2, or 4 additional O atoms adsorbed in a vanadyl configuration on top of the fivefold coordinated V. For the latter two cases, our preferred structures agree with the models of an earlier DFT study by Mellan and Grau-Crespo [22]. Decreasing the coverage from $\frac{1}{2}$ to $\frac{1}{4}$ ML (one adsorbed oxygen atom), every second oxygen atom is removed from the remaining oxygen row. Blue, orange, pink, and red lines mark the oxygen-rich ring superstructures, including V_4O_{13} (ring), V_5O_{14} (ring zigzag and ring), and V_5O_{15} stoichiometries, as depicted in Figs. 11(d), 11(f), S8(a), and S8(b) in the Supplemental Material [32], respectively. Furthermore, gray dashed lines represent the reduced ring structures obtained by removing the undercoordinated orange oxygens in Fig. 11(c), leading to the V_4O_{12} and V_4O_{11} surface stoichiometries. Structures and simulated STM images of different ring terminations are presented in the Supplemental Material [32]. The plot also shows the stability limit of the VO_2 phase with respect to the vanadium pentoxide as a vertical black solid line defined as the enthalpy of the following reaction: $2\text{VO}_2 + \frac{1}{2}\text{O}_2 \rightarrow \text{V}_2\text{O}_5$. For calculating this phase boundary, the experimental heats of formation of the VO_2 and V_2O_5 phases with respect to vanadium metal [52,53] were used. It should be noted that the calculated phase

boundary strongly depends on the chosen functional and spin treatment due to the peculiarities of an appropriate treatment of the VO_2 phase [39].

Over a wide range of chemical potentials, the ring structure with V_4O_{13} [Fig. 11(d)] and the zigzag with V_5O_{14} [Figs. 11(f) and 11(g)] surface stoichiometry are the most stable configurations. An unreconstructed, buckled $\text{VO}_2(110)_T$ surface, partially covered with O atoms, would be stable under strongly reducing conditions (oxygen chemical potential < -2.05 eV).

IV. DISCUSSION

In this paper, we clearly show that the lowest-energy state of the VO_2 surface in a wide range of chemical potentials is a reconstruction distinctly different from a bulk-terminated surface. The unreconstructed rutile $(110)_T$ termination is found only after mild annealing of a sputter-treated surface. After equilibration at higher temperatures, an adlayer with a (2×2) double-row superstructure is observed. The superstructure is slightly oxygen rich according to XPS (Fig. 8), and our data indicate that the excess oxygen is probably diffusing from the bulk to the surface at high temperatures. This would lead to slight stoichiometry variations in the bulk, which should be easily possible, considering the reducibility of vanadium(IV). While the (2×2) periodicity is consistent with previous reports [23,26], the simple models proposed earlier [22] that invoke only adsorption of excess O are neither supported by the STM measurements nor by the DFT calculations.

The DFT models explain the main features of the STM images. The calculations showed that the aligned bright spots of the experimentally observed double rows are related to the ring structure in Fig. 11(d), which is the most stable surface termination at an oxygen chemical potential of -1.54 eV and higher. The model assigns the experimental double rows in Figs. 6 to O atoms at the apex of VO_4 tetrahedra. In the range of chemical potentials between -1.54 and -2.05 eV, another ring structure [Fig. 11(f,g)], which exhibits a zigzag pattern like the features observed in Fig. 6(b), is more stable.

The stability of the ring terminations, especially at chemical potentials corresponding to higher oxygen pressures, is related to both the fact that the ring structure contains more oxygen than the adsorption phases and also to the close relationship of the ring structure to a vanadium pentoxide monolayer whose surface energy is only $11 \text{ meV}/\text{\AA}^2$ according to our calculations, far below that of $\text{VO}_2(110)_T$ (Table II). This relationship is not only structural—as we pointed out, the ring structures were derived from a V_2O_5 monolayer—but also evident in the electronic structure. As shown in Fig. 13, the projected density of states (pDOS) onto vanadium and oxygen atomic orbitals of the ring phase of Fig. 11(d) compares well with the V_2O_5 bulk pDOS. The graphs show that, unlike the rutile VO_2 phase, V_2O_5 as well as the V_4O_{13} ring displays a band gap where the V $3d$ band is separated by 1.9 and 2.2 eV from the O $2p$ band, respectively. It should be noted that the calculation for the V_2O_5 phase underestimates the experimental band gap of 2.2–2.4 eV [54–56], and therefore, we also expect a similar underestimation for the surface phase.

While we find similar stability for the oxygen adsorption phases on the $\text{VO}_2(110)_T$ surface as discussed by Mellan and

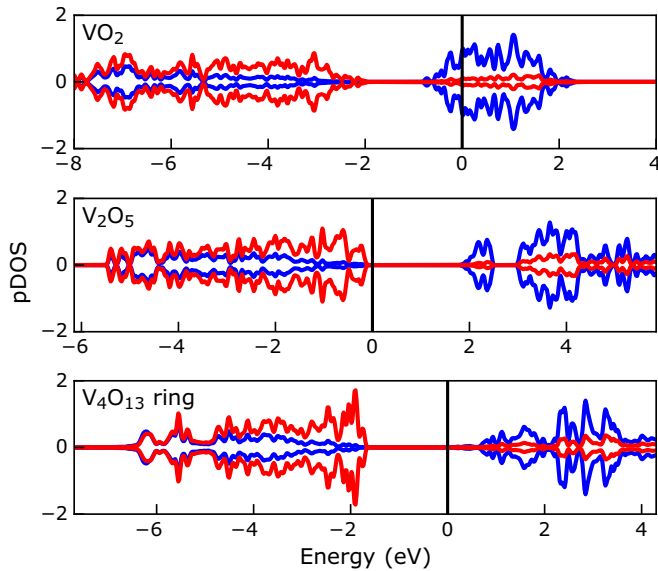


FIG. 13. The (SCAN) projected density of states (pDOS) onto vanadium and oxygen atomic orbitals in the rutile VO_2 and V_2O_5 bulk phases compared with the V_4O_{13} ring termination. The DOS is given states per eV and colored in red and blue for O and V, respectively. The bands are aligned with respect to the upper edge of the O $2p$ band. The black vertical line denotes the Fermi level, which is determined by the VO_2 substrate in the case of the ring termination and drawn at the valence band maximum for V_2O_5 .

Grau-Crespo [22], reconstructions were not considered in that computational study. Considering that a simple adsorption phase cannot explain the atomically resolved STM measurements in this paper, we conclude that the ring terminations are central building blocks for an atomistic understanding of the surface termination of $\text{VO}_2(110)_T$.

Comparing our favored model [Fig. 11(d)] and STM simulations with the experimental STM images (Fig. 7), we find that the alignment of the bright spots confirms that the holes in the experimental images revealing the bare (1×1) surface are a double layer below the ring surface structure. However, the experimental apparent height difference in STM (1.6 \AA) is much smaller than the calculated geometrical thickness of the double layer (5.4 \AA). This might be explained by the insulating nature of the V_4O_{13} surface layer.

Not all experimental features are captured in the present model, however. Firstly, experimental STM images show additional bright spots between the double rows that are not explained by the V_4O_{13} ring termination (ovals in Figs. 6 and S5 in the Supplemental Material [32]). Secondly, the double rows in the experiment are always aligned with respect to the neighboring row like in Figs. 6(a) and 6(b). Our present model also allows hexagonal rings that form the double-row pattern to be shifted by half of the superstructure cell in the $[001]$ direction; this is not observed in the experiment. The reason for observing only the aligned pattern is not evident from the DFT model. Probably, the alignment is caused by the entities forming the additional bright spots between the double rows. Although the exact origin of these spots has not been identified, we suspect that the undercoordinated oxygen atoms in the lower part of the surface layer

[V = O vanadyl groups, left side of the circle in Fig. 11(d)] could be a favored adsorption site. This could cause the experimentally observed protrusions, and linking two vanadyl oxygens of adjacent rows by some (unknown) species would also explain the alignment of neighboring double rows.

Nevertheless, the ring structures with the V_4O_{13} and V_5O_{14} surface stoichiometries constitute a structural basis that explains the most prominent features of the experimentally observed surface reconstruction. However, a considerable amount of potentially stable surface structures exists, with only subtle energy differences between them. A further exploration remains a challenging task for the near future, see Ref. [39].

The presence of an insulating surface phase supported on a metallic bulk also raises the question whether this affects the MIT. As discussed earlier, tetrahedral ring terminations have a very different electronic structure compared with the bulk: First, due to the crystal field splitting, the energies of the V t_{2g} and e_g manifolds are exchanged, and second, a higher oxygen concentration empties the V $3d$ band and makes the layer insulating. Following an argument that was already brought forward in Ref. [23], the electronic correlations in the ring layers are not expected to play a significant role due to the lack of occupied V $3d$ states. Moreover, the DFT calculations reveal that the ring terminations also lower the occupation number of the V $3d$ band in the subsurface layer by 20–50% with respect to the bare $\text{VO}_2(110)_T$ surface [57] depending on the stoichiometry of the ring structure. This may also lead to suppression of the MIT near the surface.

The surface reconstruction itself is quite flexible and may sustain the transition to the insulating phase without fragmenting. However, the presence of an insulating surface layer needs to be considered when using this material, e.g., in surface sensitive methods such as angle-resolved photoemission spectroscopy or when interfacing with other materials. Even though the reconstruction may not remain intact when growing an epitaxial film on top, the interface could stay oxygen rich or nonstoichiometric in contrast to the growth of heterostructures with bulk-terminated interfaces.

V. SUMMARY

In summary, in this paper, we present a comprehensive study on the surface properties of VO_2 single crystals, employing imaging, diffraction, and spectroscopy techniques complemented by DFT calculations. The crystals exhibit the expected bulk structures below and above the MIT. Their most stable surface, assigned to $(0\bar{1}\bar{1})$ and (110) in the monoclinic and tetragonal structure, respectively, was investigated in detail. Impurities show strong variations even within individual samples but do not affect the described results, except for a minority superstructure with $c(4 \times 2)$ symmetry attributed to Cs atoms that seems to limit the extent of the (2×2) phase. Comparison of XPS spectra acquired in grazing and normal emission shows that the surface is oxygen rich. The distinctly different XPS peak shapes reflect the drastic change in electronic structure that accompanies the MIT.

The most prominent outcome of this paper is the description of a (2×2) surface phase structurally distinct from the VO_2 bulk-terminated surface. The proposed ring models are

based on corner-sharing tetrahedra and pyramids, structurally and electronically related to V_2O_5 layers. This implies that surface atoms are in a markedly different environment than the bulk atoms, likely with profound influence on the surface properties, such as oxygen adsorption or the temperature of the MIT of nanoparticles of this exciting material.

ACKNOWLEDGMENTS

Support by the Austrian Science Fund FWF, Projects No. V 773-N (Elise-Richter-Stelle) and No. Z 250-N27 (Wittgenstein Prize), is gratefully acknowledged. The authors

further thank Andrey Prokofiev and Flora Pötzleitner for Laue backscattering and initial XPS measurements, respectively.

The samples were synthesized by L.A.B. STM and LEED measurements were performed by M.W. XPS measurements were done by M.W. and B.S.J.H. Trace analysis measurements were done by A.L. XRD was applied by J.L. The experimental data were analyzed by M.W., B.S.J.H., F.M., H.-P.S., and M.S. DFT calculations were performed by J.P. and analyzed by J.P., F.M., M.S., and J.R. All authors discussed the data and contributed to the paper. M.W., J.P., F.M., and U.D. wrote the paper. U.D. and F.M. oversaw the project.

-
- [1] F. J. Morin, Oxides Which Show a Metal-to-Insulator Transition at the Neel Temperature, *Phys. Rev. Lett.* **3**, 34 (1959).
- [2] A. C. Jones, S. Berweiger, J. Wei, D. Cobden, and M. B. Raschke, Nano-optical investigations of the metal–insulator phase behavior of individual VO_2 microcrystals, *Nano Lett.* **10**, 1574 (2010).
- [3] J. H. Park, J. M. Coy, T. S. Kasirga, C. Huang, Z. Fei, S. Hunter, and D. H. Cobden, Measurement of a solid-state triple point at the metal-insulator transition in VO_2 , *Nature (London)* **500**, 431 (2013).
- [4] Z. Shao, X. Cao, H. Luo, and P. Jin, Recent progress in the phase-transition mechanism and modulation of vanadium dioxide materials, *NPG Asia Mater.* **10**, 581 (2018).
- [5] M. F. Becker, A. B. Buckman, R. M. Walser, T. Lépine, P. Georges, and A. Brun, Femtosecond laser excitation of the semiconductor-metal phase transition in VO_2 , *Appl. Phys. Lett.* **65**, 1507 (1994).
- [6] S. Lysenko, N. Kumar, A. Rúa, J. Figueroa, J. Lu, and F. Fernández, Ultrafast structural dynamics of VO_2 , *Phys. Rev. B* **96**, 075128 (2017).
- [7] M. F. Jager, C. Ott, P. M. Kraus, C. J. Kaplan, W. Pouse, R. E. Marvel, R. F. Haglund, D. M. Neumark, and S. R. Leone, Tracking the insulator-to-metal phase transition in VO_2 with few-femtosecond extreme UV transient absorption spectroscopy, *Proc. Natl Acad. Sci.* **114**, 9558 (2017).
- [8] J. I. Sohn, H. J. Joo, D. Ahn, H. H. Lee, A. E. Porter, K. Kim, D. J. Kang, and M. E. Welland, Surface-stress-induced Mott transition and nature of associated spatial phase transition in single crystalline VO_2 nanowires, *Nano Lett.* **9**, 3392 (2009).
- [9] K. Shibuya, M. Kawasaki, and Y. Tokura, Metal-insulator transition in epitaxial $V_{1-x}W_xO_2$ ($0 \leq x \leq 0.33$) thin films, *Appl. Phys. Lett.* **96**, 022102 (2010).
- [10] A. Yano, H. Clarke, D. G. Sellers, E. J. Braham, T. E. G. Alivio, S. Banerjee, and P. J. Shamberger, Toward high-precision control of transformation characteristics in VO_2 through dopant modulation of hysteresis, *J. Phys. Chem. C* **124**, 21223 (2020).
- [11] H. Yoon, M. Choi, T.-W. Lim, H. Kwon, K. Ihm, J. K. Kim, S.-Y. Choi, and J. Son, Reversible phase modulation and hydrogen storage in multivalent VO_2 epitaxial thin films, *Nat. Mater.* **15**, 1113 (2016).
- [12] A. Cavalleri, C. Tóth, C. W. Siders, J. A. Squier, F. Ráksi, P. Forget, and J. C. Kieffer, Femtosecond Structural Dynamics in VO_2 During an Ultrafast Solid-Solid Phase Transition, *Phys. Rev. Lett.* **87**, 237401 (2001).
- [13] M. J. Lee, Y. Park, D.-S. Suh, E.-H. Lee, S. Seo, D.-C. Kim, R. Jung, B.-S. Kang, S.-E. Ahn, C. B. Lee, D. H. Seo, Y.-K. Cha, I.-K. Yoo, J.-S. Kim, and B. H. Park, Two series oxide resistors applicable to high speed and high density nonvolatile memory, *Adv. Mater.* **19**, 3919 (2007).
- [14] D. Lee, J. Lee, K. Song, F. Xue, S.-Y. Choi, Y. Ma, J. Podkaminer, D. Liu, S.-C. Liu, B. Chung, W. Fan, S. J. Cho, W. Zhou, J. Lee, L.-Q. Chen, S. H. Oh, Z. Ma, and C.-B. Eom, Sharpened VO_2 phase transition via controlled release of epitaxial strain, *Nano Lett.* **17**, 5614 (2017).
- [15] E. Strelcov, Y. Lilach, and A. Kolmakov, Gas sensor based on metal-insulator transition in VO_2 nanowire thermistor, *Nano Lett.* **9**, 2322 (2009).
- [16] N. Shukla, A. V. Thathachary, A. Agrawal, H. Paik, A. Aziz, D. G. Schlom, S. K. Gupta, R. Engel-Herbert, and S. Datta, A steep-slope transistor based on abrupt electronic phase transition, *Nat. Commun.* **6**, 2 (2015).
- [17] Z. Qu, L. Yao, Y. Zhang, B. Jin, J. He, and J. Mi, Surface and interface engineering for VO_2 coatings with excellent optical performance: From theory to practice, *Mater. Res. Bull.* **109**, 195 (2019).
- [18] N. Wang, Y. K. Peh, S. Magdassi, and Y. Long, Surface engineering on continuous VO_2 thin films to improve thermochromic properties: Top-down acid etching and bottom-up self-patterning, *J. Colloid Interf. Sci.* **512**, 529 (2018).
- [19] Y. Muraoka and Z. Hiroi, Metal-insulator transition of VO_2 thin films grown on TiO_2 (001) and (110) substrates, *Appl. Phys. Lett.* **80**, 583 (2002).
- [20] Z. Yu, Y. Liu, Z. Zhang, M. Cheng, Z. Zou, Z. Lu, D. Wang, J. Shi, and R. Xiong, Controllable phase transition temperature by regulating interfacial strain of epitaxial VO_2 films, *Ceram. Int.* **46**, 12393 (2020).
- [21] T. D. Manning, I. P. Parkin, M. E. Pemble, D. Sheel, and D. Vernardou, Intelligent window coatings: atmospheric pressure chemical vapor deposition of tungsten-doped vanadium dioxide, *Chem. Mater.* **16**, 744 (2004).
- [22] T. A. Mellan and R. Grau-Crespo, Density functional theory study of rutile VO_2 surfaces, *J. Chem. Phys.* **137**, 154706 (2012).

- [23] M. J. Wahila, N. F. Quackenbush, J. T. Sadowski, J.-O. Krisponeit, J. I. Flege, R. Tran, S. P. Ong, C. Schlueter, T.-L. Lee, M. E. Holtz, D. A. Muller, H. Paik, D. G. Schlom, W.-C. Lee, and L. F. J. Piper, The breakdown of Mott physics at VO₂ surfaces, [arXiv:2012.05306](https://arxiv.org/abs/2012.05306) (2020).
- [24] N. F. Quackenbush, H. Paik, M. E. Holtz, M. J. Wahila, J. A. Moyer, S. Barthel, T. O. Wehling, D. A. Arena, J. C. Woicik, D. A. Muller, D. G. Schlom, and L. F. J. Piper, Reducing orbital occupancy in VO₂ suppresses Mott physics while Peierls distortions persist, *Phys. Rev. B* **96**, 081103(R) (2017).
- [25] J.-O. Krisponeit, S. Fischer, S. Esser, V. Moshnyaga, T. Schmidt, L. F. J. Piper, J. I. Flege, and J. Falta, The morphology of VO₂/TiO₂(001): Terraces, facets, and cracks, *Sci. Rep.* **10**, 22374 (2020).
- [26] S. Fischer, J.-O. Krisponeit, M. Foerster, L. Aballe, J. Falta, and J. Ingo Flege, Massively strained VO₂ thin film growth on RuO₂, *Cryst. Growth Des.* **20**, 2734 (2020).
- [27] I. Kylänpää, J. Balachandran, P. Ganesh, O. Heinonen, P. R. C. Kent, and J. T. Krogel, Accuracy of *ab initio* electron correlation and electron densities in vanadium dioxide, *Phys. Rev. Materials* **1**, 065408 (2017).
- [28] W. H. Brito, M. C. O. Aguiar, K. Haule, and G. Kotliar, Metal-Insulator Transition in VO₂: A DFT + DMFT Perspective, *Phys. Rev. Lett.* **117**, 056402 (2016).
- [29] J. Schoiswohl, S. Surnev, F. P. Netzer, and G. Kresse, Vanadium oxide nanostructures: From zero- to three-dimensional, *J. Phys. Condens. Matter* **18**, R1 (2006).
- [30] C. Klein, G. Kresse, S. Surnev, F. P. Netzer, M. Schmid, and P. Varga, Vanadium surface oxides on Pd(111): a structural analysis, *Phys. Rev. B* **68**, 235416 (2003).
- [31] R.-P. Blum, H. Niehus, C. Hucho, R. Fortrie, M. V. Ganduglia-Pirovano, J. Sauer, S. Shaikhutdinov, and H.-J. Freund, Surface Metal-Insulator Transition on a Vanadium Pentoxide (001) Single Crystal, *Phys. Rev. Lett.* **99**, 226103 (2007).
- [32] See Supplemental Material at <http://link.aps.org/supplemental/10.1103/PhysRevMaterials.5.125001> for the following topics: (1) Experimental: Bulk characterization by LA-ICP-MS, Structural characterization of the crystals by XRD and Laue back-reflection; Additional STM data: Influence of the c(4 × 2) on the coverage of the (2 × 2) phase, Distances measured within the (2 × 2) structure for different STM contrasts, Different appearance of the (2 × 2) phase in STM; Additional XPS data: Comparison of NE and GE at different annealing temperatures, Comparison of monoclinic and tetragonal. (2) Additional DFT data: Modified ring terminations, Simulated STM images at bias from −2 V to +2 V.
- [33] O. D Rigaku, *CrysAlis PRO v38.46* (Rigaku Oxford Diffraction Ltd, Yarnton, 2017).
- [34] I. Niedermaier, C. Kolbeck, H.-P. Steinrück, and F. Maier, Dual analyzer system for surface analysis dedicated for angle-resolved photoelectron spectroscopy at liquid surfaces and interface, *Rev. Sci. Instrum.* **87**, 045105 (2016).
- [35] G. Kresse and J. Furthmüller, Efficient iterative schemes for *ab initio* total-energy calculations using a plane-wave basis set, *Phys. Rev. B* **54**, 11169 (1996).
- [36] G. Kresse and D. Joubert, From ultrasoft pseudopotentials to the projector augmented-wave method, *Phys. Rev. B* **59**, 1758 (1999).
- [37] J. Sun, A. Ruzsinszky, and J. P. Perdew, Strongly Constrained and Appropriately Normed Semilocal Density Functional, *Phys. Rev. Lett.* **115**, 036402 (2015).
- [38] B. Stahl and T. Bredow, Critical assessment of the DFT + U approach for the prediction of vanadium dioxide properties, *J. Comp. Chem.* **41**, 258 (2020).
- [39] J. Planer, F. Mittendorfer, and J. Redinger, First principles studies of the electronic and structural properties of the rutile VO₂(110) surface and its oxygen-rich terminations, *J Phys.: Condens. Matter* **33**, 475002 (2021).
- [40] H. J. Monkhorst, J. D. Pack, and J. P. Perdew, Special points for Brillouin-zone integrations, *Phys. Rev. B* **13**, 5188 (1976).
- [41] J. Tersoff and D. R. Hamann, Theory of the scanning tunneling microscope, *Phys. Rev. B* **31**, 805 (1985).
- [42] W. Brückner, Structural relations between the VO₂ phases, *Cryst. Res. Tech.* **16**, K28 (1981).
- [43] D. Kucharczyk and Z. Niklewski, Accurate x-ray determination of the lattice parameters and the thermal expansion coefficients of VO₂ near the transition temperature, *J. Appl. Cryst.* **12**, 370 (1979).
- [44] G. Silversmit, D. Depla, H. Poelman, G. B. Marin, and R. De Gryse, Determination of the V2p XPS binding energies for different vanadium oxidation states (V⁵⁺ to V⁰⁺), *J. Electron. Spectros. Relat. Phenomena* **135**, 167 (2004).
- [45] M. C. Biesinger, L. W. M. Lau, A. R. Gerson, and R. St. C. Smart, Resolving surface chemical states in XPS analysis of first row transition metals, oxides and hydroxides: Sc, Ti, V, Cu and Zn, *Appl. Surf. Sci.* **257**, 887 (2010).
- [46] D. Wegkamp, M. Herzog, L. Xian, M. Gatti, P. Cudazzo, C. L. McGahan, R. E. Marvel, R. F. Haglund, Jr., A. Rubio, M. Wolf, and J. Stähler, Instantaneous Band Gap Collapse in Photoexcited monoclinic VO₂ due to Photocarrier Doping, *Phys. Rev. Lett.* **113**, 216401 (2014).
- [47] A. Hariki, T. Uozumi, and J. Kuneš, LDA + DMFT approach to core-level spectroscopy: Application to 3d transition metal compounds, *Phys. Rev. B* **96**, 045111 (2017).
- [48] U. Diebold, J. Anderson, K.-O. Ng, and D. Vanderbilt, Evidence for the Tunneling Site on Transition-Metal Oxides: TiO₂(110), *Phys. Rev. Lett.* **77**, 1322 (1996).
- [49] H. Over, A. P. Seitsonen, E. Lundgren, M. Schmid, and P. Varga, Experimental and simulated STM images of stoichiometric and partially reduced RuO₂(110) surfaces including adsorbate, *Surf. Sci.* **515**, 143 (2002).
- [50] J. A. Enterkin, A. K. Subramanian, B. C. Russell, M. R. Castell, K. R. Poepelmeier, and L. D. Marks, A homologous series of structures on the surface of SrTiO₃(110), *Nat. Mater.* **9**, 245 (2010).
- [51] K. Reuter and M. Scheffler, Composition, structure, and stability of RuO₂(110) as a function of oxygen pressure, *Phys. Rev. B* **65**, 035406 (2001).
- [52] Thermodynamic properties of compounds, V₂O₅ to ThP, in *Landolt-Börnstein—Group IV Physical Chemistry 19A4 (Pure Substances. Part 4—Compounds from HgH_g to ZnTe_g)* (Springer-Verlag, Berlin, Heidelberg, 2001).
- [53] Thermodynamic properties of compounds, SbO₂ to Rh₂O₃, in *Landolt-Börnstein—Group IV Physical Chemistry 19A4 (Pure Substances. Part 4—Compounds from HgH_g to ZnTe_g)* (Springer-Verlag, Berlin, Heidelberg, 2001).

- [54] N. Van Hieu and D. Lichtman, Bandgap radiation induced photodesorption from V_2O_5 powder and vanadium oxide surfaces, *J. Vac. Sci. Technol.* **18**, 49 (1981).
- [55] S. F. Cogan, N. M. Nguyen, S. J. Perrotti, and R. D. Rauh, Optical properties of electrochromic vanadium pentoxide, *J. Appl. Phys.* **66**, 1333 (1989).
- [56] A. Z. Moshfegh and A. Ignatiev, Formation and characterization of thin film vanadium oxides: auger electron spectroscopy, x-ray photoelectron spectroscopy, x-ray diffraction, scanning electron microscopy, and optical reflectance studies, *Thin Solid Films* **198**, 251 (1991).
- [57] J. Planer, Surface and Bulk Characterization of Transition Metal Oxides: A density functional theory study of ZrO_2 and VO_2 , Ph.D. thesis, TU Wien, 2021.